Received: 1 December 2018 | Revised: 20 February 2019 | Accepted: 8 March 2019

DOI: 10.1111/jace.16438

ORIGINAL ARTICLE

Journal of the American Ceramic Society

Thermodynamic assessment of the hollandite high-level radioactive waste form

Stephen A. Utlak[1] | **Theodore M. Besmann**[1] | **Kyle S. Brinkman**[2,3] | **Jake W. Amoroso**[4]

[1]General Atomics Center for Nuclear Technologies, University of South Carolina, Columbia, South Carolina

[2]Department of Materials Science and Engineering, Clemson University, Clemson, South Carolina

[3]Center for Nuclear Environmental Engineering Sciences and Radioactive Waste Management (NEESRWM), Clemson University, Clemson, South Carolina

[4]Savannah River National Laboratory, Aiken, South Carolina

Correspondence
Stephen A. Utlak, General Atomics Center for Nuclear Technologies, University of South Carolina, Columbia, SC.
Email: utlak@cec.sc.edu

Funding information
U. S. Department of Energy.

Abstract

Hollandite has been studied as a candidate ceramic waste form for the disposal of high-level radioactive waste due to its inherent leach resistance and ability to immobilize alkaline-earth metals such as Cs and Ba at defined lattice sites in the crystallographic structure. The chemical and structural complexity of hollandite-type phases developed for high-level waste immobilization limits the systematic experimental research that is required to understand phase development due to the large number of potential additives and compositional ranges that must be evaluated. Modeling the equilibrium behavior of the complex hollandite-forming oxide waste system would aid in the design and processing of hollandite waste forms by predicting their thermodynamic stability. Thus, a $BaO–Cs_2O–TiO_2–Cr_2O_3–Al_2O_3–Fe_2O_3–FeO–Ga_2O_3$ thermodynamic database was developed in this work according to the CALPHAD methodology. The compound energy formalism was used to model solid solution phases such as hollandite while the two-sublattice partially ionic liquid model characterized the oxide melt. Results of model optimizations are presented and discussed including a 1473 K isothermal $BaO–Cs_2O–TiO_2$ pseudo-ternary diagram that extrapolates phase equilibrium behavior to regions not experimentally explored.

KEYWORDS

modeling/model, nuclear waste, phase equilibria, synroc, thermodynamics

1 | INTRODUCTION

Ceramic waste forms have been shown to accommodate nearly all constituents in the high-level nuclear waste (HLW) generated from reprocessing spent nuclear fuel including radioactive and non-radioactive components and are known to be resistant to hydrothermal leaching. Ceramic waste forms offer better durability and higher waste loadings for some species for which existing HLW glass formulations are inappropriate or inefficient.[1–4] Specifically, titanate ceramics, eg, SYNROC,[5] have been extensively studied for use in immobilizing nuclear wastes due to their inherent leach resistance.[6–8] Cs is one challenging radionuclide due to its thermal heat load, volatility at high temperatures, and tendency to form water-soluble compounds.[4] Ti-substituted hollandite, one of the SYNROC phases, is an alternative candidate for Cs immobilization. In these waste forms, ^{137}Cs (and other constituent radionuclides, ie ^{137}Ba, ^{87}Rb) is incorporated into the crystalline structure.[8–10] Notably, natural analogs of hollandite including ankagite are present in dolomitic marble in the Apuan Alps in Tuscany, Italy, which demonstrates the stability of the hollandite phase over geologic timescales of interest for nuclear waste immobilization.

Titanate hollandite ceramics can be generally expressed as $A_x(Ti^{+4},M)_8O_{16}$ where A represents alkali and alkaline earth metal cations such as Cs^{+1}, Ba^{+2}, Rb^{+1}, K^{+1}, and Sr^{+2} and M represents +2/+3 cations such as Al^{+3}, Fe^{+3}, Fe^{+2}, Ga^{+3}, Cr^{+3}, Zn^{+2}, and Mg^{+2}.[4,11] The structure is composed of edge and corner sharing TiO_6 and MO_6 octahedra that form a framework consisting of tunnels parallel to the *c*-axis or *b*-axis for tetragonal or monoclinic hollandites, respectively.[11] The atom positions located within the tunnel sites can be occupied by A-site cations such as Cs^{+1} and Ba^{+2}, which is beneficial as both ^{137}Cs and its decay product ^{137}Ba can remain immobilized in the hollandite structure.[12]

Studies have been conducted to analyze the effect of M-site substitution on the crystallographic structure of hollandite and Cs incorporation.[2,4,9,10,13–15] Costa et al,[12] for instance, determined that hollandite thermodynamic stability generally increased with decreasing average M-site cation radius while Aubin-Chevaldonnet et al[13] demonstrated that various M-site substitutions for Ti^{+4} affects the fraction of Cs incorporated into the hollandite tunnel sites. While experimentally assessing the effects of hollandite additives remains a focus of ongoing research, the complexity in the hollandite system limits the ability to evaluate large composition areas.

To reduce the magnitude of the possible experimental work and target specific hollandite formulations, a thermodynamic database is being developed to provide phase relations to guide development of compositions that are likely to form the hollandite phase as well as avoid secondary Cs parasitic phases. The database developed in this work according to the CALPHAD methodology[16] consists of the oxides $BaO–Cs_2O–TiO_2–Cr_2O_3–Al_2O_3–Fe_2O_3–FeO–Ga_2O_3$ and can calculate equilibrium behavior including extension to compositions/conditions that have not been experimentally determined. Solid solutions such as the hollandite phase were modeled with the compound energy formalism (CEF)[17–22] while the oxide liquid was characterized using the two-sublattice partially ionic liquid (TSPIL) model.[23,24] The oxides of Cr, Al, Fe and Ga were considered in this initial development as experimental measurements have been reported for hollandite phases containing these constituents. The hollandite CEF model will subsequently be expanded to include additional elements of interest.

2 | IDENTIFYING OXIDE SYSTEMS TO ADDRESS

Table S1 provides synthesized hollandite compositions that were used to thermodynamically assess hollandite. The molar amount of TiO_2 averages ~70% of the hollandite-forming waste system. Thus, BaO, Cs_2O, and the additive oxides are dilute with respect to TiO_2, which assures that two non-TiO_2 oxides are unlikely to interact whereas all will warrant a description of energetic interactions with TiO_2. As such, Gibbs energies for the solid phases stable in the pseudo-binary systems of the oxides of substitutional elements with TiO_2 were incorporated into the database except for Al_2O_3, Ga_2O_3, and Cr_2O_3. The $Al_2O_3–TiO_2$[25] and $Ga_2O_3–TiO_2$[26–28] systems were neglected as the intermediate compounds known to form in these systems, Al_4TiO_8, Al_2TiO_5, Ga_2TiO_5, and a series of $Ga_4Ti_{m-4}O_{2m-2}$ phases where $9 < m < 25$, are not stable at <1537 K, which is above temperatures of interest. Amoroso et al[14] fabricated hollandites with Cr_2O_3 and did not report the formation of a chromium titanate minor phase, hence the $Cr_2O_3–TiO_2$ system was also neglected. The pseudo-binary system of $Cs_2O–TiO_2$ had not previously been assessed and, consequently, a new assessment of this system was conducted.

Minor phases that were observed to form[14] also led to the inclusion of intermediate compounds in the $BaO–Fe_2O_3$ and $Al_2O_3–FeO$ systems.

3 | BACKGROUND

3.1 | $Cs_2O–TiO_2$

Schmitz-Dumont & Reckhard[29] conducted liquidus measurements for the $Cs_2Ti_2O_5–TiO_2$ system, reporting the formation of one intermediate stoichiometric compound, $Cs_2Ti_4O_9$. Grey et al,[30] however, did not observe the formation of $Cs_2Ti_4O_9$ but instead identified the compounds $Cs_2Ti_5O_{11}$ and $Cs_2Ti_6O_{13}$, which were subsequently confirmed by Grey et al,[31] Kwiatkowska et al,[32] Bursill et al,[33] Peres et al,[34] and Kobyakov et al[35] Thus, the $Cs_2Ti_4O_9$ compound, and by extension the liquidus data reported by Schmitz-Dumont & Reckhard,[29] was neglected while $Cs_2Ti_5O_{11}$ and $Cs_2Ti_6O_{13}$ were included in the assessment of the $Cs_2O–TiO_2$ system. Grey et al[30] were unable to experimentally determine the liquidus boundary in the analyzed 75-100 mol% TiO_2 region of the $Cs_2O–TiO_2$ system due to Cs volatilization, although phase transition temperatures were reported as follows: $Cs_2Ti_2O_5 + Cs_2Ti_5O_{11} \rightarrow Cs_2Ti_5O_{11}$ + melt = 1117 K, $Cs_2Ti_5O_{11}$ + melt $\rightarrow Cs_2Ti_6O_{13}$ + melt = 1373 K, and $Cs_2Ti_6O_{13}$ + melt $\rightarrow TiO_2$ + melt = 1405 K. Lu & Jin[36] summarized TiO_2 melting temperatures measured in varied atmospheres, ultimately adopting the 2185 ± 10 K melting point measured for a near stoichiometric $TiO_{1.999}$ sample in a pure oxygen atmosphere. This melting point as well as the reported 763 K Cs_2O melting temperature[37,38] were used in the $Cs_2O–TiO_2$ system assessment.

3.2 | Hollandite

Amoroso et al[2,14] fabricated hollandite phases by melt processing to determine the impact of Cr, Al, and Fe additives on the stability and melting temperature in both single-phase[14] and multi-phase (MP) studies.[2] In both, the hollandite samples were heat treated at a constant temperature of 1773 K for

20 minutes and then allowed to cool in the powered off furnace,[2,14] with cooling rates reported to drop from 60 to 15 K/min by ~1473 K.[2] While the Fe-containing single phase hollandites (SPH) completely melted, Cr–Al–Fe (CAF) SPH samples only exhibited partial melting and Cr-SPH samples did not melt at all but were instead sintered at 1773 K (Section 4.44.4).[13] Dandeneau et al[10] also fabricated a melt processed multi-phase waste form with a targeted composition equivalent to the CAF-MP composition of Amoroso et al,[2] hence the ensuing discussion is applicable to both the Amoroso et al[2] and Dandeneau et al[10] studies. The SPH study targeted three hollandite nominal compositions that were fabricated in air and a 1% H_2 reducing atmosphere,[14] which will be designated as SPH and SPHR, respectively. Ti metal and TiO_2 were also added to some samples prior to synthesis,[14] which will be designated as SPH-Ti and SPHR-Ti, respectively. Amoroso et al[14] determined the stoichiometry of the fabricated hollandite compositions through use of inductively coupled plasma (ICP) analysis as well as the minor phases that formed in addition to hollandite. The MP hollandite study conducted by Amoroso et al[2] differed from the SPH study[14] by incorporating additional oxides into samples that could be targeted by facilities operating to produce a MP ceramic waste form. The MP study targeted the same hollandite nominal compositions as the SPH study, and, consequently, the amounts of the oxides that formed the hollandite phase as listed in table 5 of Amoroso et al[2] were used as a basis in this work (Table S1). The ratio of $Fe^{+2}/(Fe^{+2} + Fe^{+3})$ for the CAF containing hollandites differed between the SPH and MP studies; thus, the SPH ratios were adopted in this work (Table S1). Also, the SPH Al_2O_3 quantities indicated in the Amoroso et al[14] table 2 footnotes were adopted. The waste compositions implemented in this work for the SPH hollandites[14] fabricated containing only the Fe additive were derived by adopting the Cr_2O_3 compositions used by Amoroso et al[2] and then substituting Fe_2O_3 and FeO for Cr_2O_3 while retaining the $Fe^{+2}/(Fe^{+2} + Fe^{+3})$ ratio of the SPH study.[14]

Xu et al[4,11] used solid state reaction and sol-gel methods to fabricate hollandites. Both studies employed final heat treatments of 1473-1523 K for 2-3 hours. Aubin-Chevaldonnet et al[13] used a solid-state reaction to form oxide pellets that were calcined and sintered at 1473 K for 30 hours in air. Costa et al[12] prepared hollandite samples by first mixing, heating, and evaporating citrate solutions before ultimately forming and heat treating pellets at 1523 K for 3 hours. Database calculations were conducted at each of these final heat treatment temperatures for comparison with the phase equilibria reported in these studies. Similarly, the reported 1473 K temperature at which the cooling rate of melt processed samples started slowing was adopted as defining the equilibrium state and, as such, calculations for comparison with melt processed sample results were conducted at this temperature. Xu et al,[4,9,11] Aubin-Chevaldonnet et al,[13] and Costa et al[12] synthesized hollandites with the additives Ga, Al, Cr, and Fe, hence the database was developed to include the oxides of these additives.

Wu et al[11] derived a standard enthalpy of formation using drop solution calorimetry for a hollandite phase with the composition $Ba_{1.18}Cs_{0.21}Al_{2.44}Ti_{5.53}O_{16.}$ Costa et al[12] employed the same approach for the $Ba_{1.24}Al_{2.48}Ti_{5.52}O_{16}$ and $Ba_{1.24}Fe_{2.48}Ti_{5.52}O_{16}$ compositions. Xu et al[4] and Wen et al[15] used density functional theory (DFT)[39,40] to calculate formation enthalpies at 0 K from the Ba to Cs endmember of two-thirds A-site occupied hollandites containing Al and Ga. The data reported by Xu et al[4] was neglected as the DFT calculations were refined with improved computational parameterization by Wen et al.[15] Additionally, Wu et al[41] measured heat capacities of a series of barium aluminotitanate hollandites including a Cs-substituted phase with the composition $Ba_{1.18}Cs_{0.21}Al_{2.44}Ti_{5.53}O_{16}$ at 1.2 mPa from 2 to 300 K.

4 | THERMODYNAMIC MODELING AND OPTIMIZATION

4.1 | CEF and TSPIL models

The thermodynamic representations were optimized using the FactSage[42] software to obtain values for the CEF and TSPIL models for the solid solutions and liquid phases. The CEF is a sublattice-based model that can account for the non-stoichiometry of a substitutional or interstitial solid solution based on lattice site occupancies, which can include vacancies and interstitial sites. An example CEF three sublattice model can be represented as:

$$(A,B)_k(D,E,F)_l(G)_m$$

where *A*-*G* are elements distributed on one of the three possible lattice sites, and the subscripts *k*, *l*, and *m* are the sublattice stoichiometric coefficients. The CEF Gibbs energy function is defined in Hillert.[21]

The TSPIL model is based on the concept that in ionic liquid phases each atom bears a charge and thus is surrounded by unlike charged atoms resulting in atomic ordering. This ordering can be treated as two sublattices, one containing only cations and the other anions, vacancies, and neutral species (C, A, Va, and B, respectively) in:

$$\left(C_i^{+\nu_i}\right)_P \left(A_j^{-\nu_j}, Va, B_k^0\right)_Q$$

where the indices *i*, *j*, and *k* represent specific sublattice constituents. The superscripts $+\nu_i$ and $-\nu_j$ represent the charge of the *i*th or *j*th cation or anion, respectively, while 0 indicates a neutral species. Electroneutrality is maintained by allowing the stoichiometric coefficients (*P* and *Q*) to vary as a function of site fractions.

As noted in Utlak & Besmann,[43] the standard molar Gibbs energy of a phase modeled using the CEF can be expressed as:

$$G_m = \Sigma \Delta_f {}^oG_{end} \Pi y_J^s + RT\Sigma\Sigma n^s y_J^s \ln y_J^s + {}^EG_m \quad (1)$$

where $\Delta_f {}^oG_{end}$ is the molar Gibbs energy of formation of an end-member, y_J^s is the site fraction of the *J*th constituent in the nth sublattice, and n^s is the stoichiometric coefficient of the *n*th sublattice. The first, second, and third terms of Equation (1) are the Gibbs energy surface of reference, ideal entropy of mixing, and excess Gibbs energy of mixing, respectively.

The excess Gibbs energy, which accounts for the departure from ideal mixing of species on the same sublattice due to attraction or repulsion of the mixing constituents,[44] can be described with a generalized regular solution expression:

$${}^EG_m = \Pi y_J^s \Sigma y_B^t L_{A,B:D:G} \ldots + \Pi y_J^s \Sigma\Sigma y_B^t y_D^u L_{A,B:D,E:G} \ldots + \ldots \quad (2)$$

where the subscripts A, B, D, E, and G as well as superscripts *t* and *u* refer to the constituents in a sublattice and the sublattice designations, respectively, in a generalized CEF formulation for a three sublattice phase $(A,B)_k^t (D,E,F)_l^u (G)_m^v$. The subscripts *k*, *l*, and *m* in the generalized formula represent the sublattice stoichiometric coefficients. The commas separating constituents in the interaction parameter designations of Equation (2) indicate the interactions between constituents on the same sublattice, whereas the colons separate sublattices. Equation (2) can be expanded to describe, in principle, constituent interactions of a multicomponent system of any order.

The interaction parameters of Equation (2) can be expressed as a Redlich-Kister (RK) power series[16] in terms of site fractions. As an example, for a binary interaction between the A and B species of Equation (2):

$$L_{A,B:D:G} = \sum_{k=0}^{n} {}^kL_{A,B:D:G} \left(y_A - y_B\right)^k \quad (3)$$

where D and G are constituents on each of the second and third sublattices, *y* represents the site fraction of the subscripted sublattice constituent, and *k* is the order of the expansion. The interaction parameter *L* on the right-hand side of Equation (3) can be expressed as a polynomial in temperature with the form:

$${}^kL_{A,B:D:G} = A + B \cdot T + C \cdot T \ln(T) + D \cdot T^2 + E \cdot T^3 + F \cdot T^{-1} \quad (4)$$

where *T* is the temperature in kelvin and the variables *A*, *B*, *C*, *D*, *E*, and *F* are coefficients determined by optimizing the model Gibbs energy function to thermochemical and/or phase equilibria data. In practice, only the *A* and *B* coefficients of Equation (4) are generally needed in an assessment unless experimental data can justify additional coefficients.[16]

The molar Gibbs energy in the TSPIL model is:

$$\begin{aligned} G_m = {} & \sum\sum y_{C_i} y_{A_j} {}^oG_{C_i:A_j} + Q\left(y_{Va} \sum y_{C_i} {}^oG_{C_i} + \sum y_{B_k} {}^oG_{B_k}\right) \\ & + RT\left[P \sum y_{C_i} \ln y_{C_i} + Q\left(\sum y_{A_j} \ln y_{A_j} + y_{Va} \ln y_{Va} + \sum y_{B_k} \ln y_{B_k}\right)\right] + {}^EG_m \end{aligned} \quad (5)$$

where ${}^oG_{C_i:A_j}$ is the Gibbs energy of formation for $\nu_i + \nu_j$ moles of atoms of the end-member C_iA_j while ${}^oG_{C_i}$, and ${}^oG_{B_k}$ are the values for C_i and B_k, respectively. The first, second, and third terms of Equation (5) are the Gibbs energy surface of reference for all possible types of constituents, the random configurational entropy on each sublattice, and the excess Gibbs mixing energy, which can be expressed as:

$$\begin{aligned} {}^EG_m = {} & \sum\sum\sum y_{i_1} y_{i_2} y_j L_{i_1,i_2:j} \\ & + \sum\sum\sum y_i y_{j_1} y_{j_2} L_{i:j_1,j_2} + \sum\sum y_i y_{j_1} y_{Va} L_{i:j_1,Va} + \ldots \end{aligned} \quad (6)$$

The interaction parameters again can be expressed as a Redlich-Kister power series (Equation (3)).

4.2 | Stoichiometric phases

As observed by Hanaor & Sorrell[45] based on the results of cited studies, rutile is the equilibrium polymorph of TiO_2. Hence, a Gibbs energy description of the rutile polymorph has been incorporated in the database (Table S2). Intermediate stoichiometric phases for the BaO–TiO_2,[36] Cs_2O–TiO_2,[29,30] FeO–TiO_2,[46] and Fe_2O_3–TiO_2[47] systems were included in the database. In addition, Amoroso et al[14] observed the formation of the $BaFe_{12}O_{19}$ and $FeAl_2O_4$ phases. Consequently, these phases as well as the remaining intermediate line compounds known to be stable in the BaO–Fe_2O_3[48] system were also incorporated into the database (Table S2). While the only intermediate phase in the Al_2O_3–FeO[49–54] system, $FeAl_2O_4$, has previously been represented as a stoichiometric compound and a solid solution, in this work a line compound was assumed, which is a sufficient approximation as $FeAl_2O_4$ is a minor phase due to the low of Al_2O_3 and FeO content in relevant waste compositions (Table S1). Values from the FactSage 7.2 databases cited in Table S2 from sources such as NIST-JANAF thermochemical tables[55] were used with slight modifications as necessary from the assessments.

The three stoichiometric compounds $Cs_2Ti_2O_5$, $Cs_2Ti_5O_{11}$, and $Cs_2Ti_6O_{13}$ were optimized as part of the Cs_2O–TiO_2 system assessment. The Neumann-Kopp rule[56] was applied to derive endmember heat capacities and estimated values for standard entropies with the latter values confirmed to be within the entropic range predicted by Latimer's method.[57,58] Standard formation enthalpies were optimized to the phase equilibria data discussed in Section 3.13.1.

The $CsAlTiO_4$ and $Cs_2AlGaTi_2O_8$ line compounds were observed to form as secondary phases in Ba–Cs–Fe and Bs–Cs–Ga hollandites fabricated by Amoroso et al[14] and Aubin-Chevaldonnet et al,[13] respectively, and thus, included in the database. Gibbs energy functions for the $CsAlTiO_4$ and $Cs_2AlGaTi_2O_8$ phases were determined from heat capacities and standard entropies derived in the same manner as those for the cesium titanate compounds. Standard enthalpies of formation were then optimized to allow experimentally observed phase assemblages to be computed to form.

4.3 | Hollandite solid solution

The hollandite sublattice model was developed to coincide with the hollandite general formula[13,14]:

$$\left(Ba_x Cs_y\right)\left(M,Ti\right)^{+2,+3,+4}_{2x+y}\left(Ti\right)^{+4}_{8-2x-y}O_{16},\ x+y<2$$

where M represents a divalent, trivalent, or tetravalent cation, which resulted in the CEF four sublattice formalism:

$$\left(Ba^{+2},Cs^{+1},Va\right)^{\alpha}_{2}\left[Ti^{+4},Cr^{+3},Al^{+3},Fe^{+3},Fe^{+2},Ga^{+3}\right]^{\beta}_{4}\left\{Ti^{+4}\right\}_{4}\left\langle O^{-2}\right\rangle_{16}$$

As $x + y < 2$, the first and second sublattice stoichiometric coefficients of 2 and 4, respectively, bound all potential stoichiometric values of the first and second general formula terms (Ba_xCs_y) and $(M,Ti)^{+2,+3,+4}_{2x+y}$, respectively. The second and third sublattice stoichiometric coefficients sum to eight to be consistent with the hollandite crystallographic tunnel sites composed of octahedrally-coordinated M-site cations.[4,13] Thus, with the variation of sublattice species site fractions, the hollandite CEF model encompasses the range of possible hollandite compositions.

4.3.1 | Optimization of hollandite CEF model

The Neumann-Kopp rule[56] was applied to derive endmember heat capacities and estimated values for standard entropies with the latter values also approximated by the entropic range predicted by Latimer's method.[57,58] Endmember standard formation enthalpies (Table S3) were then optimized to the hollandite targeted compositions of the studies discussed in Section 3.23.2 for the respective waste compositions listed in Table S1. An example of the Gibbs energy relation for a neutral endmember such as $Ba_2Fe_4Ti_4O_{16}$ as generated by this approach is seen in Equation (7).

$$\begin{aligned}{}^{o}G_{Ba_2Fe_4Ti_4O_{16}} = {} & 2{}^{o}G_{BaO(s)} + 2{}^{o}G_{Fe_2O_3(s)} \\ & + 4{}^{o}G_{TiO_2(s)} + \Delta H_{opt,298.15K}\end{aligned} \tag{7}$$

where ${}^{o}G$ represents the Gibbs energy function of a specified oxide and $\Delta H_{opt,298.15K}$ is the standard enthalpy obtained from optimization to experimental data.

Gibbs energies of charged endmembers were defined as per the example of Equation (8) for function of a specified oxide and $Cs_2Al_4Ti_4O_{16}^{-2}$ function of a specified oxide and.

$$\begin{aligned}{}^{o}G_{Cs_2Al_4Ti_4O_{16}^{-2}} = {} & {}^{o}G_{Cs_2O(s)} + 2{}^{o}G_{Al_2O_3(s)} + 4{}^{o}G_{TiO_2(s)} + \\ & 2{}^{o}G_{Ti_3O_5(s)} - 3{}^{o}G_{Ti_2O_3(s)} + \Delta H_{opt,298.15K}\end{aligned} \tag{8}$$

where ${}^{o}G_{Ti_3O_5(s)}$ and ${}^{o}G_{Ti_2O_3(s)}$ were included to obtain the correct oxygen stoichiometry and oxidation state.

Six RK parameters in the hollandite CEF were used to obtain representative Gibbs energy functions for the targeted compositions. Equation (9) defines the 298 K molar Gibbs energy function of the optimized hollandite solid solution with endmember and RK parameter values listed in Table S3.

$$\begin{aligned}G_m^{\text{hollandite}} = {} & y^{\alpha}_{Ba^{+2}} y^{\beta}_{Ti^{+4}} {}^{o}G_{Ba_2Ti_8O_{16}^{+4}} + y^{\alpha}_{Cs^{+1}} y^{\beta}_{Ti^{+4}} {}^{o}G_{Cs_2Ti_8O_{16}^{+2}} + y^{\alpha}_{Va} y^{\beta}_{Ti^{+4}} {}^{o}G_{Ti_8O_{16}} \\ & + y^{\alpha}_{Ba^{+2}} y^{\beta}_{Cr^{+3}} {}^{o}G_{Ba_2Cr_4Ti_4O_{16}} + y^{\alpha}_{Cs^{+1}} y^{\beta}_{Cr^{+3}} {}^{o}G_{Cs_2Cr_4Ti_4O_{16}^{-2}} + y^{\alpha}_{Va} y^{\beta}_{Cr^{+3}} {}^{o}G_{Cr_4Ti_4O_{16}^{-4}} \\ & + y^{\alpha}_{Ba^{+2}} y^{\beta}_{Al^{+3}} {}^{o}G_{Ba_2Al_4Ti_4O_{16}} + y^{\alpha}_{Cs^{+1}} y^{\beta}_{Al^{+3}} {}^{o}G_{Cs_2Al_4Ti_4O_{16}^{-2}} + y^{\alpha}_{Va} y^{\beta}_{Al^{+3}} {}^{o}G_{Al_4Ti_4O_{16}^{-4}} \\ & + y^{\alpha}_{Ba^{+2}} y^{\beta}_{Fe^{+3}} {}^{o}G_{Ba_2Fe_4Ti_4O_{16}} + y^{\alpha}_{Cs^{+1}} y^{\beta}_{Fe^{+3}} {}^{o}G_{Cs_2Fe_4Ti_4O_{16}^{-2}} + y^{\alpha}_{Va} y^{\beta}_{Fe^{+3}} {}^{o}G_{Fe_4Ti_4O_{16}^{-4}} \\ & + y^{\alpha}_{Ba^{+2}} y^{\beta}_{Fe^{+2}} {}^{o}G_{Ba_2Fe_4Ti_4O_{16}^{-4}} + y^{\alpha}_{Cs^{+1}} y^{\beta}_{Fe^{+2}} {}^{o}G_{Cs_2Fe_4Ti_4O_{16}^{-6}} + y^{\alpha}_{Va} y^{\beta}_{Fe^{+2}} {}^{o}G_{Fe_4Ti_4O_{16}^{-8}} \\ & + y^{\alpha}_{Ba^{+2}} y^{\beta}_{Ga^{+3}} {}^{o}G_{Ba_2Ga_4Ti_4O_{16}} + y^{\alpha}_{Cs^{+1}} y^{\beta}_{Ga^{+3}} {}^{o}G_{Cs_2Ga_4Ti_4O_{16}^{-2}} + y^{\alpha}_{Va} y^{\beta}_{Ga^{+3}} {}^{o}G_{Ga_4Ti_4O_{16}^{-4}} \\ & + RT\left(y^{\alpha}_{Ba^{+2}} \ln y^{\alpha}_{Ba^{+2}} + 2y^{\alpha}_{Cs^{+1}} \ln y^{\alpha}_{Cs^{+1}} + 2y^{\alpha}_{Va} \ln y^{\alpha}_{Va} + 4y^{\beta}_{Ti^{+4}} \ln y^{\beta}_{Ti^{+4}} + 4y^{\beta}_{Cr^{+3}} \ln y^{\beta}_{Cr^{+3}}\right. \\ & \left. + 4y^{\beta}_{Al^{+3}} \ln y^{\beta}_{Al^{+3}} + 4y^{\beta}_{Fe^{+3}} \ln y^{\beta}_{Fe^{+3}} + 4y^{\beta}_{Fe^{+2}} \ln y^{\beta}_{Fe^{+2}} + 4y^{\beta}_{Ga^{+3}} \ln y^{\beta}_{Ga^{+3}}\right) \\ & + y^{\alpha}_{Cs^{+1}} y^{\alpha}_{Va} y^{\beta}_{Cr^{+3}} {}^{0}L_{Cs^{+1},Va:Cr^{+3}:Ti^{+4}:O_2^{-2}} + y^{\alpha}_{Cs^{+1}} y^{\alpha}_{Va} y^{\beta}_{Al^{+3}} {}^{0}L_{Cs^{+1},Va:Al^{+3}:Ti^{+4}:O_2^{-2}} \\ & + y^{\alpha}_{Cs^{+1}} y^{\alpha}_{Va} y^{\beta}_{Fe^{+3}} {}^{0}L_{Cs^{+1},Va:Fe^{+3}:Ti^{+4}:O_2^{-2}} + y^{\alpha}_{Cs^{+1}} y^{\beta}_{Cr^{+3}} y^{\beta}_{Fe^{+3}} {}^{0}L_{Cs^{+1}:Cr^{+3},Fe^{+3}:Ti^{+4}:O_2^{-2}} \\ & + y^{\alpha}_{Cs^{+1}} y^{\beta}_{Al^{+3}} y^{\beta}_{Fe^{+3}} {}^{0}L_{Cs^{+1}:Al^{+3},Fe^{+3}:Ti^{+4}:O_2^{-2}} + y^{\alpha}_{Ba^{+2}} y^{\beta}_{Cr^{+3}} y^{\beta}_{Fe^{+2}} {}^{0}L_{Ba^{+2}:Cr^{+3},Fe^{+2}:Ti^{+4}:O_2^{-2}}\end{aligned} \tag{9}$$

4.4 | Liquid phase of hollandite-forming system

As discussed in Section 3.23.2, the hollandite sample fabrication methods of solid state reaction, sol-gel, and combustion synthesis with final sintering at temperatures of l473-1523 K for 3-30 hours did not provide liquid phase data.[4,11–13] Hence, the liquid phase was not addressed. Additionally, while Amoroso et al[14] noted that Fe-containing samples exhibited signs of melting when melt processing was attempted, inspection of CAF samples indicated only near or partial melting occurred, and Cr-containing samples showed minimal signs of melting, formed largely from solid state reactions. Thus, only solid state behavior of the CAF and Cr samples was considered.

As the Fe samples were not rapidly quenched but instead allowed to naturally cool in the powered off furnace,[14] the phases observed were deemed to be the equilibrium state assemblage.

4.4.1 | Liquid phase of Cs_2O–TiO_2 system

While it was largely unnecessary to assess the melts for the constituent systems, the exception was Cs_2O–TiO_2. A TSPIL model was required to allow consideration of the liquid phase as the solidus/liquidus values were useful in generating the molar Gibbs energies of the intermediate stoichiometric phases. The liquid phase was modeled such that Cs^{+1} and Ti^{+4} cations appear on the first sublattice and the O^{-2} anion resides on the second sublattice:

$$\left(CS^{+1}, Ti^{+4}\right)_P \left(O^{-2}\right)_Q$$

Grey et al[30] were unable to measure liquidus data due to high Cs volatility, and the liquidus data reported by Schmitz-Dumont & Reckhard[29] was neglected as the measurements indicated the formation of $Cs_2Ti_4O_9$, which did not agree with other experimental studies of the C_2O–TiO_2 system.[30–35] As such, estimation of the Cs_2O–TiO_2 liquidus curve was required, which was based on the analogous K_2O–TiO_2 phase diagram reported by Eriksson & Pelton.[46] As K_2O and Cs_2O are alkali metal oxides with no polymorphs, it is reasonable to assume that the phase equilibrium behavior of the Cs_2O–TiO_2 system can be generally approximated by the K_2O–TiO_2 system. Inspection of the K_2O–TiO_2 phase diagram computed by Eriksson & Pelton[46] indicates that the liquidus curve continuously decreases from 100-36 mol% TiO_2. Intermediate line compounds at TiO_2 mol fractions >50% are seen to melt incongruently, and a eutectic point forms at 20 mol% TiO_2. The TSPIL model for the Cs_2O–TiO_2 system was optimized to agree with the trends exhibited by the K_2O–TiO_2 phase diagram, which required a single RK parameter(values listed in Table S3).

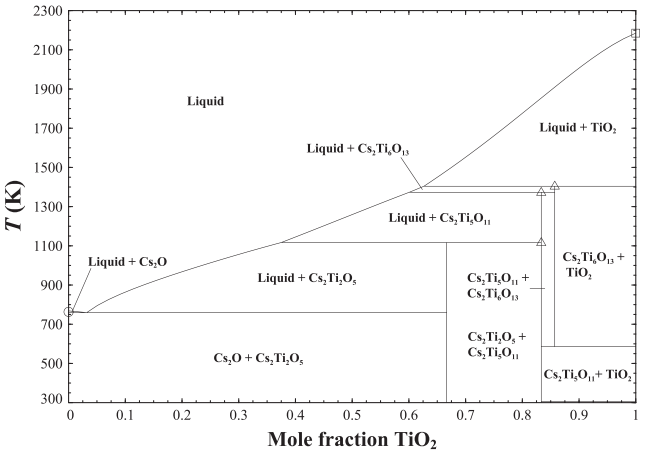

FIGURE 1 Computed Cs_2O–TiO_2 pseudo-binary phase diagram with experimental measurements shown as points. Data: ○[38] □[36] △[30]

$$\begin{aligned} G_m^{\text{liquid}} = & y_{Cs^{+1}} y_{O^{-2}} {}^{o}G_{Cs^{+1}:O^{-2}} + y_{Ti^{+4}} y_{O^{-2}} {}^{o}G_{Ti^{+4}:O^{-2}_2} \\ & + RT\left(2y_{O^{-2}}\left(y_{Cs^{+1}} \ln y_{Cs^{+1}} + y_{Ti^{+4}} \ln y_{Ti^{+4}}\right)\right. \\ & \left. + \left(y_{Cs^{+1}} + 4y_{Ti^{+4}}\right)\left(y_{O^{-2}} \ln y_{O^{-2}}\right)\right) \\ & + y_{Cs^{+1}} y_{Ti^{+4}} y_{O^{-2}} {}^{0}L_{Cs^{+1},Ti^{+4}:O^{-2}_2} \end{aligned} \quad (10)$$

5 | RESULTS AND DISCUSSION

5.1 | Cs_2O–TiO_2 pseudo-binary system

The available Cs_2O–TiO_2 crystalline phase data consists of $Cs_2Ti_2O_5$, $C_2Ti_5O_{11}$, and $Cs_2Ti_6O_{13}$ incongruent melting temperatures as well as the Cs_2O and TiO_2 congruent melting temperatures. The phase diagram resulting from the combined optimizations of the liquid, $Cs_2Ti_2O_5$, $C_2Ti_5O_{11}$, and $Cs_2Ti_6O_{13}$ Gibbs energy functions (Figure 1) indicates that all melting temperatures were well reproduced. Altogether with the analogous features of the K_2O–TiO_2 phase diagram.

5.2 | Thermodynamic database of hollandite-forming oxide system

Results of the hollandite CEF optimizations are displayed in Tables 1 and 2, which contain targeted, measured, and calculated hollandite compositions (Table 1) as well as calculated mass fractions of secondary phases (Table 2). Experimentally observed secondary phases for each composition are also listed in Table 2. Database calculations to determine non-melt processed hollandite compositions were conducted at the temperatures listed in Table 1, which are sintering temperatures for hollandite pellets fabricated in the studies discussed in Section 3.23.2. Again, the reported 1473 K temperature at which the

TABLE 1 Targeted, measured, and calculated hollandite phase compositions for specified waste types

Waste type	*T* (K)	Targeted composition	Measured composition	Calculated composition[a]
Fe-SPH-1[14]	1473	$Ba_{1.0}Cs_{0.3}Fe_{2.3}Ti_{5.7}O_{16}$	$Ba_{1.0}Cs_{0.16}Fe_{2.4}Ti_{5.8}O_{15.9}$	$Ba_{1.04}Cs_{0.047}Fe_{1.74}Al_{0.357}Ti_{5.90}O_{16}$
Fe-SPHR[14]	1473	$Ba_{1.0}Cs_{0.3}Fe_{2.3}Ti_{5.7}O_{16}$	$Ba_{1.0}Cs_{0.14}Fe_{2.4}Ti_{5.7}O_{15.0}$	$Ba_{1.14}Cs_{0.105}Fe_{0.80}Al_{0.781}Ti_{6.42}O_{16}$
Fe-SPH-Ti[14]	1473	$Ba_{1.0}Cs_{0.3}Fe_{2.3}Ti_{5.7}O_{16}$	$Ba_{1.0}Cs_{0.24}Fe_{2.4}Ti_{5.6}O_{15.8}$	$Ba_{1.08}Cs_{0.027}Fe_{1.97}Al_{0.210}Ti_{5.83}O_{16}$
Cr-SPH-1[14]	1473	$Ba_{1.0}Cs_{0.3}Cr_{2.3}Ti_{5.7}O_{16}$	$Ba_{1.0}Cs_{0.14}Cr_{2.3}Ti_{5.8}O_{16.2}$	$Ba_{1.04}Cs_{0.153}Cr_{2.15}Al_{0.069}Fe_{0.013}Ti_{5.77}O_{16}$
Cr-SPHR[14]	1473	$Ba_{1.0}Cs_{0.3}Cr_{2.3}Ti_{5.7}O_{16}$	$Ba_{1.0}Cs_{0.19}Cr_{2.3}Ti_{5.8}O_{15.0}$	$Ba_{1.05}Cs_{0.145}Cr_{2.14}Al_{0.084}Fe_{0.014}Ti_{5.77}O_{16}$
Cr-SPH-Ti[14]	1473	$Ba_{1.0}Cs_{0.3}Cr_{2.3}Ti_{5.7}O_{16}$	$Ba_{1.0}Cs_{0.15}Cr_{2.4}Ti_{5.6}O_{16.1}$	$Ba_{0.981}Cs_{0.213}Cr_{2.05}Al_{0.092}Fe_{0.026}Ti_{5.83}O_{16}$
Cr-SPHR-Ti[14]	1473	$Ba_{1.0}Cs_{0.3}Cr_{2.3}Ti_{5.7}O_{16}$	$Ba_{1.0}Cs_{0.19}Cr_{2.4}Ti_{5.7}O_{14.9}$	$Ba_{1.01}Cs_{0.178}Cr_{2.06}Al_{0.116}Fe_{0.013}Ti_{5.81}O_{16}$
CAF-SPH-1[14]	1473	$Ba_{1.0}Cs_{0.3}Cr_{1.0}Al_{0.3}Fe_{1.0}Ti_{5.7}O_{16}$	$Ba_{1.0}Cs_{0.16}Cr_{1.0}Al_{0.3}Fe_{1.0}Ti_{5.8}O_{16.1}$	$Ba_{0.968}Cs_{0.150}Cr_{0.900}Al_{0.397}Fe_{0.761}Ti_{5.94}O_{16}$
CAF-SPHR[14]	1473	$Ba_{1.0}Cs_{0.3}Cr_{1.0}Al_{0.3}Fe_{1.0}Ti_{5.7}O_{16}$	$Ba_{1.0}Cs_{0.15}Cr_{1.0}Al_{0.4}Fe_{1.0}Ti_{5.7}O_{15.6}$	$Ba_{1.06}Cs_{0.135}Cr_{1.27}Al_{0.471}Fe_{0.258}Ti_{6.00}O_{16}$
CAF-SPH-Ti[14]	1473	$Ba_{1.0}Cs_{0.3}Cr_{1.0}Al_{0.3}Fe_{1.0}Ti_{5.7}O_{16}$	$Ba_{1.0}Cs_{0.16}Cr_{1.1}Al_{0.4}Fe_{1.0}Ti_{5.7}O_{16.1}$	$Ba_{0.893}Cs_{0.226}Cr_{0.775}Al_{0.411}Fe_{0.805}Ti_{6.01}O_{16}$
CAF-SPHR-Ti[14]	1473	$Ba_{1.0}Cs_{0.3}Cr_{1.0}Al_{0.3}Fe_{1.0}Ti_{5.7}O_{16}$	$Ba_{1.0}Cs_{0.17}Cr_{0.9}Al_{0.6}Fe_{1.0}Ti_{5.7}O_{15.2}$	$Ba_{0.901}Cs_{0.153}Cr_{0.907}Al_{0.93}Fe_{0.059}Ti_{6.10}O_{16}$
Ga-SPH-1[4]	1523	$Ba_{1.33}Ga_{2.66}Ti_{5.34}O_{16}$	$Ba_{1.39}Ga_{2.6}Ti_{5.4}O_{16}$ $Ba_{1.3}Ga_{2.7}Ti_{5.3}O_{16.0}$	$Ba_{1.33}Ga_{2.66}Ti_{5.34}O_{16}$
Ga-SPH-2[4]	1523	$Ba_{1.04}Cs_{0.24}Ga_{2.32}Ti_{5.68}O_{16}$	$Ba_{1.09}Cs_{0.229}Ga_{2.6}Ti_{5.68}O_{16}$ $Ba_{1.1}Cs_{0.2}Ga_{2.4}Ti_{5.7}O_{16.0}$	$Ba_{1.04}Cs_{0.240}Ga_{2.32}Ti_{5.68}O_{16}$
Ga-SPH-3[4]	1523	$Ba_{0.667}Cs_{0.667}Ga_{2}Ti_{6}O_{16}$	$Ba_{0.77}Cs_{0.529}Ga_{2.06}Ti_{6}O_{16}$ $Ba_{0.7}Cs_{0.5}Ga_{2.1}Ti_{6.0}O_{16.1}$	$Ba_{0.667}Cs_{0.667}Ga_{2.00}Ti_{6.00}O_{16}$
Ga-SPH-4[4]	1523	$Cs_{1.33}Ga_{1.33}Ti_{6.67}O_{16}$	$Cs_{1.22}Ga_{1.44}Ti_{6.67}O_{16}$ $Cs_{1.2}Ga_{1.4}Ti_{6.6}O_{16.0}$	$Cs_{1.33}Ga_{1.33}Ti_{6.67}O_{16}$
Al-SPH-1[11]	1473	$Ba_{1.18}Cs_{0.21}Al_{2.44}Ti_{5.53}O_{16}$	$Ba_{1.18}Cs_{0.21}Al_{2.44}Ti_{5.53}O_{16}$	$Ba_{1.13}Cs_{0.213}Al_{2.47}Ti_{5.53}O_{16}$
Al-SPH-2[13]	1473	$Ba_{1.16}Al_{2.32}Ti_{5.68}O_{16}$	$Ba_{1.18}Al_{2.32}Ti_{5.67}O_{16}$	$Ba_{1.16}Al_{2.32}Ti_{5.68}O_{16}$
Cr-SPH-2[13]	1473	$Ba_{1.16}Cr_{2.32}Ti_{5.68}O_{16}$	$Ba_{1.16}Cr_{2.29}Ti_{5.70}O_{16}$	$Ba_{1.21}Cr_{2.42}Ti_{5.58}O_{16}$
Ga-SPH-5[13]	1473	$Ba_{1.16}Ga_{2.32}Ti_{5.68}O_{16}$	$Ba_{1.18}Ga_{2.30}Ti_{5.68}O_{16}$	$Ba_{1.16}Ga_{2.32}Ti_{5.68}O_{16}$
Fe-SPH-2[13]	1473	$Ba_{1.16}Fe_{2.32}Ti_{5.68}O_{16}$	$Ba_{1.13}Fe_{2.32}Ti_{5.70}O_{16}$	$Ba_{1.16}Fe_{2.32}Ti_{5.68}O_{16}$
AF-SPH-1[13]	1473	$Ba_{1.28}Al_{1.64}Fe_{0.92}Ti_{5.44}O_{16}$	$Ba_{1.29}Al_{1.71}Fe_{0.93}Ti_{5.38}O_{16}$	$Ba_{1.28}Al_{1.64}Fe_{0.920}Ti_{5.44}O_{16}$
AG-SPH-1[13]	1473	$Ba_{1.28}Al_{1.64}Ga_{0.92}Ti_{5.44}O_{16}$	$Ba_{1.29}Al_{1.65}Ga_{0.85}Ti_{5.48}O_{16}$	$Ba_{1.28}Al_{1.64}Ga_{0.920}Ti_{5.44}O_{16}$
Al-SPH-3[13]	1473	$Ba_{1.11}Cs_{0.10}Al_{2.32}Ti_{5.68}O_{16}$	$Ba_{1.17}Cs_{0.05}Al_{2.30}Ti_{5.67}O_{16}$ $Ba_{1.22}Cs_{0.01}Al_{2.49}Ti_{5.52}O_{16}$	$Ba_{1.11}Cs_{0.10}Al_{2.32}Ti_{5.68}O_{16}$
Cr-SPH-3[13]	1473	$Ba_{1.04}Cs_{0.24}Cr_{2.32}Ti_{5.68}O_{16}$	$Ba_{1.08}Cs_{0.11}Cr_{2.10}Ti_{5.86}O_{16}$ $Ba_{1.11}Cs_{0.06}Cr_{2.09}Ti_{5.86}O_{16}$	$Ba_{1.04}Cs_{0.240}Cr_{2.32}Ti_{5.68}O_{16}$
Ga-SPH-6[13]	1473	$Ba_{1.04}Cs_{0.24}Ga_{2.32}Ti_{5.68}O_{16}$	$Ba_{1.15}Cs_{0.15}Ga_{2.45}Ti_{5.55}O_{16}$	$Ba_{1.04}Cs_{0.240}Ga_{2.32}Ti_{5.68}O_{16}$
AG-SPH-2[13]	1473	$Ba_{1.00}Cs_{0.28}Al_{1.46}Ga_{0.82}Ti_{5.72}O_{16}$	$Ba_{1.05}Cs_{0.24}Al_{1.41}Ga_{0.76}Ti_{5.78}O_{16}$	$Ba_{1.03}Cs_{0.165}Al_{1.44}Ga_{0.784}Ti_{5.77}O_{16}$
Fe-SPH-3[13]	1473	$Ba_{1.04}Cs_{0.24}Fe_{2.32}Ti_{5.68}O_{16}$	$Ba_{1.06}Cs_{0.26}Fe_{2.28}Ti_{5.70}O_{16}$ $Ba_{1.10}Cs_{0.24}Fe_{2.35}Ti_{5.65}O_{16}$ $Ba_{0.97}Cs_{0.21}Fe_{2.23}Ti_{5.79}O_{16}$	$Ba_{1.04}Cs_{0.240}Fe_{2.32}Ti_{5.68}O_{16}$
AF-SPH-2[13]	1473	$Ba_{1.00}Cs_{0.28}Al_{1.46}Fe_{0.82}Ti_{5.72}O_{16}$	$Ba_{1.05}Cs_{0.25}Al_{1.43}Fe_{0.98}Ti_{5.74}O_{16}$ $Ba_{1.08}Cs_{0.21}Al_{1.45}Fe_{0.84}Ti_{5.69}O_{16}$ $Ba_{1.00}Cs_{0.28}Al_{1.44}Fe_{0.79}Ti_{5.76}O_{16}$	$Ba_{1.03}Cs_{0.153}Al_{1.37}Fe_{0.848}Ti_{5.78}O_{16}$
Al-SPH-4[12]	1523	$Ba_{1.24}Al_{2.48}Ti_{5.52}O_{16}$	$Ba_{1.3\pm0.07}Al_{2.4\pm0.1}Ti_{5.6\pm0.3}O_{16.0\pm0.3}$ $Ba_{1.259\pm0.004}Al_{2.24\pm0.04}Ti_{5.69\pm0.01}O_{16.01\pm0.04}$	$Ba_{1.24}Al_{2.48}Ti_{5.52}O_{16}$
Fe-SPH-4[12]	1523	$Ba_{1.24}Fe_{2.48}Ti_{5.52}O_{16}$	$Ba_{1.27\pm0.06}Fe_{2.4\pm0.1}Ti_{5.6\pm0.3}O_{16.0\pm0.3}$ $Ba_{1.236\pm0.003}Fe_{2.42\pm0.01}Ti_{5.57\pm0.02}O_{16.00\pm0.02}$	$Ba_{1.24}Fe_{2.48}Ti_{5.52}O_{16}$

[a]Compositions computed at 1 atm.

cooling rate of melt processed samples started slowing was adopted as the equilibrium temperature. Equilibrium calculations using assessed thermochemical models and values predict the hollandite phase is stable for the experimental compositions of Amoroso et al,[14] Xu et al,[9,11] Aubin-Chevaldonnet et al,[13] and Costa et al[12] (Table 1).

Analysis of the optimization results for the hollandite phases fabricated by Amoroso et al[14] indicates that calculated stoichiometries overall agree well with measured compositions with minor deviations for melt processed samples. As discussed by Amoroso et al,[14] melt processed hollandite samples prepared with Fe_2O_3 contained FeO and Al_2O_3 either from the crucible used to prepare the sample or added to the batch in the case of CAF samples, which caused $FeAl_2O_4$ to precipitate. Regardless, the computed phase equilibria confirm the observation of secondary phase $FeAl_2O_4$ in all Fe-containing waste types (Table 2). Amoroso et al[14] concluded that the Fe and CAF hollandite samples would be deficient in Fe and thus drive the hollandite compositions off stoichiometry, which was observed in all Fe- and CAF-SPH computed compositions (Table 1). It was experimentally observed that the addition of Cr and a Ti/TiO_2 buffer stabilized the hollandite structure and increased Cs incorporation.[14] The enhancement of Cs content can be ascribed to the suppression of the formation of the parasitic Cs secondary phase $CsAlTiO_4$.[14] Equilibrium calculations confirmed these experimental results as $CsAlTiO_4$ was not stable for any Cr-SPH formulations, and the Cr-SPH-Ti and CAF-SPH-Ti hollandites tolerated more Cs than the other respective melt processed waste compositions. Secondary phase formation was suppressed in hollandite compositions containing solely Cr as an additional element with only excess TiO_2 observed in samples.[14] Computations generally agreed with TiO_2 forming along with minor amounts of Cr_2O_3 (Table 2). In contrast, melt processed Fe and CAF waste types were observed to precipitate titanate and aluminate phases as well as possibly $CsAlTiO_4$.[14] Equilibrium calculations generally agreed as Fe waste type compositions yielded titanate and aluminate phases as well as TiO_2 and $CsAlTiO_4$ while the CAF waste types were computed to predominantly form TiO_2 and $FeAl_2O_4$ as secondary phases (Table 2). XRD measurements conducted by Amoroso et al[14] detected a precipitated $CsAlTiO_4$ phase in only one of the four CAF samples, and thus a computed result indicating $CsAlTiO_4$ is not stable in these systems is reasonable. Similarly, as $BaFe_{12}O_{19}$ was not detected by SEM analysis, the lack of the computed $BaFe_{12}O_{19}$ phase in Fe-SPHR and CAF-SPHR compositions was deemed reasonable.

Computed hollandite phase stoichiometries agreed well with targeted and/or measured hollandite phase compositions fabricated by Xu et al,[9,11] Aubin-Chevaldonnet et al,[13] and Costa et al[12] (Table 1). Aubin-Chevaldonnet et al[13] reported that Ba and Cs containing hollandite samples with only the Al^{+3} or Cr^{+3} substitutional elements contained only a fraction of the Cs targeted. A possible cause of this result noted by Aubin-Chevaldonnet et al[13] was that a high fraction of Cs vaporized during the solid-state reaction synthesis process and caused formation of low density samples. Comparatively, the Al-SPH-1 hollandites fabricated by Xu et al[11] via a sol-gel method had the expected Cs content. Thus, the equivalency of the calculated and targeted Al-SPH-3 Cs fraction is acceptable (Table 1).[13,14] Also, good agreement of computed results with the Cr-SPH measured compositions by Amoroso et al[14] indicates that the hollandite model accurately reflects the less than expected Cs content observed by Amoroso et al[14] and Aubin-Chevaldonnet et al.[13]

Secondary phases computed to form were generally consistent with experimental observations for non-melt processed waste types (Table 2). The $CsGaSi_{0.4}Ti_{0.6}O_4$ phase that was observed by Aubin-Chevaldonnet et al[13] to precipitate in the Ga-SPH-6 hollandite was omitted in equilibrium calculations as it was likely due to SiO_2 contamination from the silicate glass-ceramic balls used in an attrition mill as noted by the authors. The $CsAl_{0.5}Ga_{0.5}TiO_4$ phase, however, was included in the assessment of the AG-SPH-2 hollandite with the calculated result indicating that the parasitic compound reduced the fraction of Cs expected in the hollandite phase, which agreed with the experimental result (Table 1). Al-SPH-1 was experimentally observed to have no secondary phases while Al-SPH-3 with a similar composition was reported to form $Ba_2Ti_9O_{20}$ and TiO_2 alongside hollandite.[11,13] A barium titanate phase, $BaTiO_3(\beta)$, was calculated to be stable for this general composition. While Fe_2TiO_5 and $BaTi_4O_9$ were identified as minor phases in Fe-SPH-3 prepared with zirconia/silicate glass-ceramic attritor balls. Aubin-Chevaldonnet et al[13] reported that $BaTi_4O_9$ was not detected and the amount of Fe_2TiO_5 decreased in samples milled with yttrium-stabilized zirconia attritor balls, which indicates that the formation of these secondary phases was affected by sample preparation. Given these issues, it is reasonable that Fe-SPH-3 is computed to be single phase. The three minor phases containing Y, Zr, O; Cs, Si, O; and Al, O in AF-SPH-2 were likely a result of contamination from the attritor mill glass-ceramic balls as discussed by Aubin-Chevaldonnet et al.[13] However, as the AF-SPH-2 composition is similar to the melt processed Fe and CAF compositions but without Cr to suppress $CsAlTiO_4$ formation (Table S1), a relatively minor amount of $CsAlTiO_4$ is calculated to be stable (Table 2). Computations determined Cs was incorporated in the AF-SPH-2 hollandite composition and thus are consistent with experimental observations.

Table S1 lists the component compositions assumed in computing standard enthalpies of formation for comparison with experimental measurements and DFT results (Table S3). Waste types for this purpose are identified with the label inclusion of DS (drop solution) or DFT. Measured/

TABLE 2 Calculated secondary phase amounts as well as experimentally observed secondary phases that were stable for each waste type

Waste Type[a]	Phase mass fraction[b] (%)								Experimentally observed secondary phases
	TiO_2(s)	$FeAl_2O_4$(s)	$CsAlTiO_4$(s)	$Cs_2AlGaTi_2O_8$(s)	$FeTi_2O_5$(s)	$BaTiO_3$(β)	Al_2O_3(corundum)	Cr_2O_3(s)	
Fe-SPH-1[14]	13.5	10.1	2.66	0	0	0	0.559	0	$Fe_2Ti_3O_9$, $Fe_3Ti_3O_{10}$, $CsAlTiO_4$
Fe-SPHR[14]	0	14.8	1.16	0	18.4	0	0	0	$BaFe_{12}O_{19}$, $Fe_3Ti_3O_{10}$, $CsAlTiO_4$, $FeAl_2O_4$
Fe-SPH-Ti[14]	22.2	5.90	3.96	0	0	0	11.8	0	$Fe_3Ti_3O_{10}$, $CsAlTiO_4$
Cr-SPH-1[14]	16.6	0	0	0	0	0	0	2.00	TiO_2
Cr-SPHR[14]	16.2	0	0	0	0	0	0	2.42	TiO_2
Cr-SPH-Ti[14]	23.7	0	0	0	0	0	0	1.62	TiO_2
Cr-SPHR-Ti[14]	25.2	0	0	0	0	0	0	2.11	TiO_2
CAF-SPH-1[14]	10.4	3.74	0	0	0	0	0.202	1.02	Fe_2TiO_4
CAF-SPHR[14]	13.2	11.4	0	0	0	0	0	0	Fe_2TiO_4, $FeAl_2O_4$, $BaFe_{12}O_{19}$, $CsAlTiO_4$
CAF-SPH-Ti[14]	19.1	1.48	0	0	0	0	0	1.60	TiO_2, $CsAlTiO_4$
CAF-SPHR-Ti[14]	14.2	13.0	0	0	0	0	0.674	0	Fe_2TiO_4, $CsAlTiO_4$
Ga-SPH-1[4]	0	0	0	0	0	0	0	0	None detected
Ga-SPH-2[4]	0	0	0	0	0	0	0	0	None detected
Ga-SPH-3[4]	0	0	0	0	0	0.014	0	0	None detected
Ga-SPH-4[4]	0	0	0	0	0	0	0	0	Ti-rich phase
Al-SPH-1[11]	0	0	0	0	0	1.96	0	0	None detected
Al-SPH-2[13]	0	0	0	0	0	0	0	0	None detected
Cr-SPH-2[13]	3.27	0	0	0	0	0	0	0	None detected
Ga-SPH-5[13]	0	0	0	0	0	0	0	0	None detected
Fe-SPH-2[13]	0	0	0	0	0	0	0	0	None detected
AF-SPH-1[13]	0	0	0	0	0	0	0	0	None detected
AG-SPH-1[13]	0	0	0	0	0	0	0	0	None detected
Al-SPH-3[13]	0	0	0	0	0	0	0	0	TiO_2, $Ba_2Ti_9O_{20}$
Cr-SPH-3[13]	0	0	0	0	0	0	0	0	None detected
Ga-SPH-6[13]	0	0	0	0	0	0	0	0	$CsGaSi_{0.4}Ti_{0.6}O_4$
AG-SPH-2[13]	0	0	0	4.37	0	0	0	0	$CsAl_{0.5}Ga_{0.5}TiO_4$
Fe-SPH-3[13]	0	0	0	0	0	0	0	0	Fe_2TiO_5, $BaTi_4O_9$
AF-SPH-2[13]	0	0	4.56	0	0	0	0	0	Phases containing Y, Zr, Cs, Si, Al, O
Al-SPH-4[12]	0	0	0	0	0	0	0	0	None detected
Fe-SPH-4[12]	0	0	0	0	0	0	0	0	None detected

[a]Waste types correspond with compositions listed in Table S1

[b]Remaining mass fraction for each waste type consists of the hollandite phase such that the total mass fraction sums to 100%.

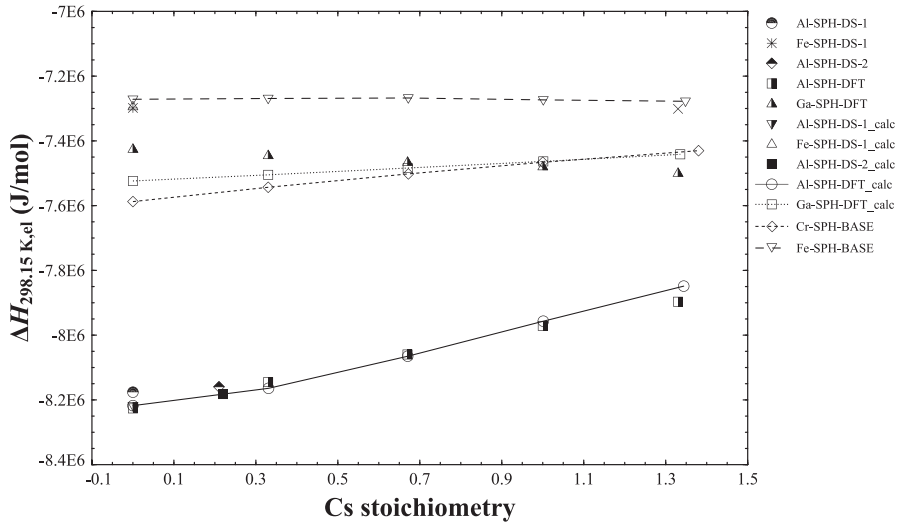

FIGURE 2 Computed hollandite standard enthalpies of formation from constituent elements compared with experimental and density functional theory derived values. Legend corresponds to Table S3 in which labels with "_calc" indicate values computed the from thermodynamic database

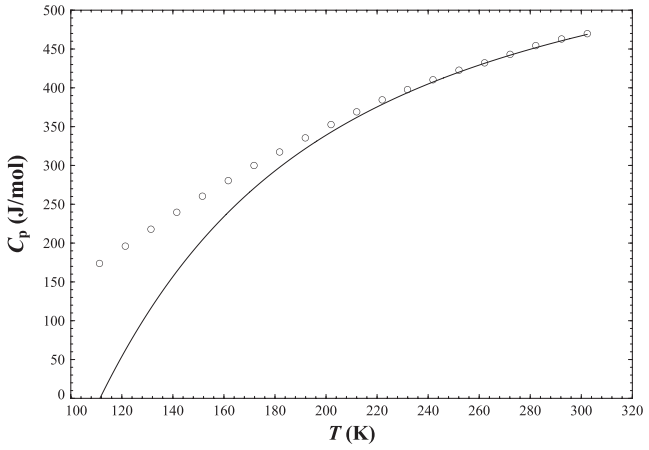

FIGURE 3 Computed heat capacity of $Ba_{1.07}Cs_{0.221}Al_{2.36}Ti_{5.64}O_{16}$ hollandite at 1.2 mPa with experimental measurements for the $Ba_{1.18}Cs_{0.21}Al_{2.44}Ti_{5.53}O_{16}$ hollandite shown as points. Data: ○[41]

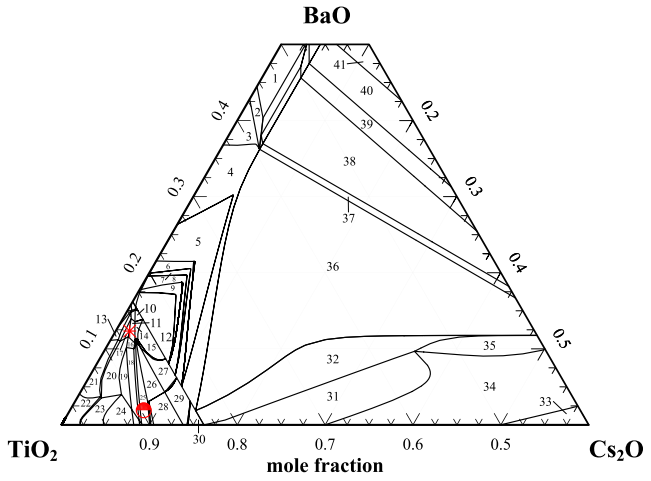

FIGURE 4 Computed 1473 K isothermal diagram of pseudo-ternary BaO–Cs_2O–TiO_2 system with oxides of Cr, Al, and Fe additives in CAF-SPH-1 quantities. Numbered phase regions are defined in Table 3

DFT derived hollandite oxide formation enthalpies were converted to molar or "elemental" enthalpies by adding the sum of the standard formation enthalpies of the constituent oxides listed in Table S3 to the Table S4 hollandite oxide formation enthalpies. Results are displayed in Table S4 as well as Figure 2.

Fe-SPH computed enthalpies were extrapolated to the $Cs_{1.35}Fe_{1.35}Ti_{6.65}O_{16}$ endmember. Computed values agree well with experimental measurements and DFT calculations for Al-SPH-DS/DFT and Fe-SPH-DS. Discrepancies exist between database calculations and Ga-SPH-DFT values near the Ba endmember with both data sets converging at a Cs stoichiometry of 1 before diverging at 1.33 (Table S4 and Figure 2). Hollandite CEF optimized parameters were generated to accurately represent measured compositions, thus Ga-SPH-DFT_calc enthalpy values are a result of targeting the Ga-SPH-1-5 and AG-SPH-1/2 compositions. Further adjustment of CEF Ga-containing endmembers would cause disagreement in Ga-SPH compositions; hence a compromise was required to obtain reasonable values of calculated compositions and experimental and DFT derived formation enthalpies. The Cr-SPH-BASE Cs endmember extends to a stoichiometric Cs value of 1.38, which is also a result of a compromise requiring adjustment of the ${}^{o}G_{Cs_2Cr_4Ti_4O_{16}^{-2}}$ endmember optimized standard formation enthalpy to approximate the $Cs_{1.33}Ga_{1.33}Ti_{6.67}O_{16}$ composition for the Cr-SPH-BASE-5 waste type while suppressing $CsAlTiO_4$ formation in the melt processed Cr-SPH waste types.

As discussed in Section 3.23.2, Wu et al[41] measured the heat capacity at a constant pressure of 1.2 mPa for the hollandite phase $Ba_{1.18}Cs_{0.21}Al_{2.44}Ti_{5.53}O_{16}$. Figure 3 displays

TABLE 3 Stable phases displayed in the isothermal $BaO–Cs_2O–TiO_2$ diagram with Cr, Al, and Fe additives (Figure 4)

Region	Stable phases[a]	Region	Stable phases	Region	Stable phases
1	H + AF + A + BT2 + C2 + BT1	15	H + C2 + FT3	29	H + FT2 + C2
2	H + AF + A + C2 + BT1	16	H + AF + C1 + FT3	30	H + C2 + F1
3	H + A + C2 + BT1	17	H + AF + FT3 + T	31	H + C2 + L + F1
4	H + C2 + BT1	18	H + C1 + FT3	32	H + C2 + L
5	H + BT5 + C2 + BT1	19	H + C1 + FT3 + T	33	H + C1 + C2 + F2 + L + F1
6	H + BT5 + C2	20	H + AF + C1 + FT3 + T	34	H + C1 + C2 + L + F1
7	H + BT4 + BT5 + C2	21	H + AF + A + C1 + T	35	H + C1 + C2 + L
8	H + BT4 + C2	22	H + AF + A + C1 + FT4 + T	36	H + C2 + BT1 + L
9	H + BT3 + BT4 + C2	23	H + AF + C1 + FT3 + FT4 + T	37	H + C2 + BT1 + L + F1
10	H + AF + C2	24	H + C1 + FT3 + FT4 + T	38	H + BT2 + C2 + BT1 + L + F1
11	H + AF + FT3	25	H + FT1 + C1	39	H + BT2 + C2 + L + F1
12	H + BT3 + C2 + T	26	H + FT1 + C1 + C2	40	H + BT2 + C1 + C2 + L + F1
13	H + AF + A + T	27	H + FT1 + C2	41	H + BF + BT2 + C1 + C2 + L + F1
14	H + AF + C2 + FT3	28	H + FT2 + C1 + C2		

[a]Stable phases: H = Hollandite, A = Al_2O_3(corundum), AF = $FeAl_2O_4$, BF = $Ba_2Fe_2O_5$, BT1 = $BaTiO_3(\alpha)$, BT2 = Ba_2TiO_4, BT3 = $Ba_2Ti_9O_{20}$, BT4 = $Ba_4Ti_{13}O_{30}$, BT5 = $Ba_6Ti_{17}O_{40}$, C1 = Cr_2O_3, C2 = $CsAlTiO_4$, F1 = FeO, F2 = Fe_2O_3, FT1 = $FeTiO_3$, FT2 = Fe_2TiO_4, FT3 = $FeTi_2O_5$, FT4 = Fe_2TiO_5, T = TiO_2, L = Liquid.

the computed hollandite heat capacity for the Al-SPH-C_p composition (Table S1), which consists of the oxides BaO, Cs_2O, TiO_2, and Al_2O_3 in amounts representative of the hollandite stoichiometry $Ba_{1.18}Cs_{0.21}Al_{2.44}Ti_{5.53}O_{16}$. Although a minor amount of Al_2O_3(corundum) and $BaTiO_3(\beta)$ is computed to form with hollandite at this composition, the minimal stoichiometric difference from that measured phase was negligible, providing good agreement between measured and computed heat capacity values. The low temperature is due to extrapolating heat capacity functions of component oxides below 298 K which is outside of the reported range for the values (Section 4.3.14.3).

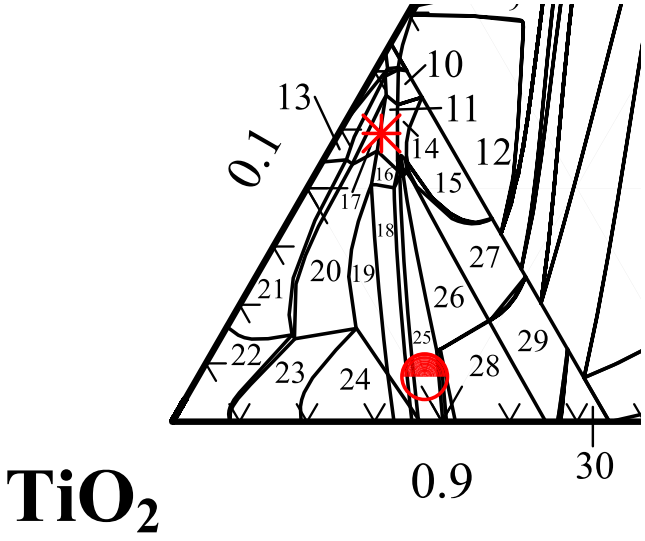

FIGURE 5 Expanded section of 1473 K of pseudo-ternary $BaO–Cs_2O–TiO_2$ isothermal diagram of Figure 4

5.3 | Extrapolation of hollandite compositions

A main benefit of thermochemical models of phases is the ability to extrapolate system behavior to compositional regions that have not been experimentally evaluated.[16] The developed database was so used to generate a 1473 K isothermal $BaO–Cs_2O–TiO_2$ pseudo-ternary diagram (Figure 4) containing Cr_2O_3, Al_2O_3, Fe_2O_3, and FeO in amounts equivalent to CAF-SPH-1 (Table S1). The diagram phase regions have been defined in Table 3. Due to the complexity of Figure 4, the smaller regions were not separately identified. Figure 5 displays an expanded section of Figure 4 in the high TiO_2, low BaO and Cs_2O region.

TABLE 4 Stable phases and amounts of and symbols located in Figure 4

Symbol	Stable phase	Amount (g)
	Hollandite ($Ba_{0.892}Cs_{0.230}Cr_{0.786}Al_{0.573}Fe_{0.608}Ti_{6.03}O_{16}$)	93.8
	$FeTi_2O_5$	2.62
	$FeAl_2O_4$	0.723
	Hollandite ($Ba_{0.143}Cs_{1.25}Cr_{0.295}Al_{0.659}Fe_{0.577}Ti_{6.47}O_{16}$)	94.7
	Cr_2O_3	4.52
	$FeTi_2O_5$	3.17

The database development approach described in Section 22 was designed to yield detailed equilibrium calculations in the high TiO_2 and low to moderate BaO and Cs_2O mole fraction region of a BaO–Cs_2O–TiO_2 pseudo-ternary diagram. Figure 4 is thus truncated at 40 mol% TiO_2 and 60 mol% BaO and Cs_2O, which is a reasonable range to display as phase stabilities calculated beyond these mole fractions would be unreliable due to neglected secondary phases consisting exclusively of BaO, Cs_2O, and/or additive oxides.

The accurate computed phase equilibria and the relations that they embody can assist in development of hollandite-based waste sequestration phases, and most notably those that can effectively accommodate Cs. For example, Figure 4 indicates secondary phases that are likely to form within a region, yet they can be seen to not necessarily impact the effectiveness of a waste form composition. This can, however, alert the developer to compositional regions containing a parasitic Cs secondary phase(s), and thus allow design of systems that avoid their formation, thereby maximizing effective hollandite waste loading. Additionally, waste compositions likely to yield a high fraction of hollandite can be projected by targeting locations on a BaO–Cs_2O–TiO_2 isothermal diagram near a phase boundary of two regions that share hollandite as a stable phase or in a region with minimal secondary phases. Approaching a boundary results in amounts of secondary phases not stable in both regions reducing to zero close to the boundary thereby increasing the ratio of hollandite to total phases formed. The waste compositions and stable phase amounts of the Figure 4 composition points near the shared boundary of regions 11 & 17 and in region 25, which contains only the secondary phases $FeTiO_3$ and Cr_2O_3, are shown in Table S1 and Table 3, respectively. According to the results in Table 4, phases within region 11 and adjacent regions are predicted to yield 96.6 and 92.5% hollandite, respectively. While region 25 has a lower predicted hollandite yield than region 17, the hollandite phase of region 25 is calculated to contain more Cs (Table 4), of which none is lost to a Cs parasitic phase. This is thus a good example of how equilibrium calculations can be used to optimize waste loading.

6 | CONCLUSION

An assessed thermodynamic database has been developed that allows successful calculation of observed equilibrium behavior of hollandite-forming BaO–Cs_2O–TiO_2–Cr_2O_3–Al_2O_3–Fe_2O_3–FeO–Ga_2O_3 systems. The variable composition hollandite and related phases were modeled using the CEF with the TSPIL model used to represent the Cs_2O–TiO_2 system oxide melt. The assessment included titanate and aluminate compounds Gibbs energies generated in this work as well as the Cs parasitic phases $CsAlTiO_4$ and $Cs_2AlGaTi_2O_8$. The constructed database was then used to generate a partial 1473 K BaO–Cs_2O–TiO_2 pseudo-ternary diagram that included fixed fractions of additional expected waste stream elements in prospective waste-form hollandite phases. These calculations extrapolate the phase equilibrium behavior of the hollandite-forming system to regions that have not been experimentally addressed, with such capability expected to be of substantial value to the development and evaluation of waste form compositions.

Future work will involve expanding the database to include oxides of additional waste elements and related titanate phases as well as non-titanate phases. These should include the oxides ZrO_2, CaO, Eu_2O_3, Y_2O_3, among others, and complex phases such as zirconolite and/or + 2/+3 titanates to ultimately develop a database that supports the efforts on multiphase ceramic waste forms.

ACKNOWLEDGMENTS

Research was conducted by the Center for Hierarchical Waste Form Materials (CHWM), an Energy Frontier Research Center (EFRC). Research was supported by the U.S. Department of Energy, Office of Basic Energy Sciences, Division of Materials Sciences and Engineering under Award DE-SC0016574.

ORCID

Stephen A. Utlak https://orcid.org/0000-0001-8834-0760
Kyle S. Brinkman https://orcid.org/0000-0002-2219-1253

REFERENCES

1. Crum JV, Turo LA, Riley BJ, Tang M, Kossoy A. Multi-phase glass-ceramics as a waste form for combined fission products: alkalis, alkaline earths, lanthanides, and transition metals. J Am Ceram Soc. 2012;95(4):1297–303.
2. Amoroso J, Marra JC, Tang M, Lin Y, Chen FL, Su D, et al. Melt processed multiphase ceramic waste forms for nuclear waste immobilization. J Nucl Mater. 2014;454(1-3):12–21.
3. Ewing RC. Long-term storage of spent nuclear fuel. Nat Mater. 2015;14(3):252–7.
4. Xu Y, Wen Y, Grote R, Amoroso J, Nickles LS, Brinkman KS. A-site compositional effects in Ga-doped hollandite materials of the form $Ba_xCs_yGa_{2x+y}T_{i8-2x-y}O_{16}$: implications for Cs immobilization in crystalline ceramic waste forms. Sci Rep. 2016;6:1–8.
5. Vance ER, Chavara DT, Gregg DJ, Synroc A. Synroc development-past and present applications. MRS Energy Sustain. 2017;4:8.
6. Ringwood AE, Kesson SE, Ware NG, Hibberson W, Major A. Immobilization of high level nuclear reactor wastes in SYNROC. Nature. 1979;278(5701):219–23.

7. Ringwood AE, Kesson SE, Ware NG, Hibberson WO, Major A. The SYNROC process: a geochemical approach to nuclear waste immobilization. Geochem J. 1979;13(4):141–65.
8. Brinkman KS, Amoroso JW, Tang M. Crystalline ceramic waste forms: comparison of reference process for ceramic waste form fabrication. Aiken, SC: Savannah River National Laboratory; 2013.
9. Xu Y, Feygenson M, Page K, Nickles LS, Brinkman KS. Structural evolution in hollandite solid solutions across the A-site compositional range from Ba1.33Ga2.66Ti5.34O16 to Cs1.33Ga1.33Ti6.67O16. J Am Ceram Soc. 2016;99(12):4100–6.
10. Dandeneau CS, Hong T, Brinkman KS, Vance ER, Amoroso JW. Comparison of structure, morphology, and leach characteristics of multi-phase ceramics produced via melt processing and hot isostatic pressing. J Nucl Mater. 2018;502:113–22.
11. Xu H, Wu L, Zhu J, Navrotsky A. Synthesis, characterization and thermochemistry of Cs-, Rb- and Sr-substituted barium aluminium titanate hollandites. J Nucl Mater. 2015;459:70–6.
12. Costa G, Xu HW, Navrotsky A. Thermochemistry of barium hollandites. J Am Ceram Soc. 2013;96(5):1554–61.
13. Aubin-Chevaldonnet V, Caurant D, Dannoux A, Gourier D, Charpentier T, Mazerolles L, et al. Preparation and characterization of (Ba, Cs)(M, T_i)$_{8O}$16 (M = ^{Al}3+, ^{Fe}3+, ^{Ga}3+, ^{Cr}3+, ^{Sc}3+, ^{Mg}2+) hollandite ceramics developed for radioactive cesium immobilization. J Nucl Mater. 2007;366(1-2):137–60.
14. Amoroso J, Marra J, Conradson SD, Tang M, Brinkman K. Melt processed single phase hollandite waste forms for nuclear waste immobilization: Ba1.0Cs0.3A2.3Ti5.7O16; A=Cr, Fe, Al. J Alloy Compd. 2014;584:590–9.
15. Wen Y, Xu Y, Brinkman KS, Shuller-Nickles L. Atomistic scale investigation of cation ordering and phase stability in Cs-substituted $Ba_{1.33}Zn_{1.33}Ti_{6.67}O_{16}$, $Ba_{1.33}Ga_{2.66}Ti_{5.67}O_{16}$ and $Ba_{1.33}A_{l2.66}Ti_{5.33}O_{16}$ hollandite. Sci Rep. 2018;8:1–11.
16. Lukas H, Fries SG, Sundman B. Computational thermodynamics: the Calphad method, 1st edn. New York, NY: Cambridge University Press; 2007: p. 324.
17. Andersson JO, Guillermet AF, Hillert M, Jansson B, Sundman B. A compound-energy model of ordering in a phase with sites of different coordination numbers. Acta Metall Mater. 1986;34(3): 437–45.
18. Harvig H, Kullberg L, Roti I, Okinaka H, Kosuge K, Kachi S. An extended version of the regular solution model for stoichiometric phases and ionic melts. Acta Chem Scand. 1971;25: 3199–204.
19. Hillert M, Staffansson LI. Regular solution model for stoichiometric phases and ionic melts. Acta Chem Scand. 1970;24(10):3618–26.
20. Sundman B, Agren J. A regular solution model for phases with several components and sublattices, suitable for computer applications. J Phys Chem Solids. 1981;42(4):297–301.
21. Hillert M. The compound energy formalism. J Alloy Compd. 2001;320(2):161–76.
22. Hillert M. Some properties of the compound energy model. Calphad. 1996;20(3):333–41.
23. Hillert M, Jansson B, Sundman B, Agren J. A two-sublattice model for molten solutions with different tendency for ionization. Metall Trans A. 1985;16A(2):261–6.
24. Sundman B. Modification of the two-sublattice model for liquids. Calphad. 1991;15(2):109–19.
25. Jung IH, Eriksson G, Wu P, Pelton A. Thermodynamic modeling of the Al_2O_3–Ti_2O_3–TiO_2 system and its applications to the Fe–Al–Ti–O inclusion diagram. ISIJ Int. 2009;49(9):1290–7.
26. Lejus AM, Goldberg D, Revcolev A. On some new compounds formed by the TiO_2 rutile with trivalent and tetravalent metal oxides. Cr Acad Sci C Chim. 1966;263(20):1223–6.
27. Kamiya S, Tilley R. Phase relations in pseudobinary system TiO_2-Ga_2O_3. J Solid State Chem. 1977;22(2):205–16.
28. Bursill LA, Stone GG. Tunnel and intergrowth structures in the gallia-rich gallium titanate system. J Solid State Chem. 1981;38(2):149–57.
29. Schmitz-Dumont O, Reckhard H. Characterization of the Alkali Titanates. Monatsh Chem. 1959;90(2):134–42.
30. Grey IE, Madsen IC, Watts JA, Bursill LA, Kwiatkowska J. New cesium titanate layer structures. J Solid State Chem. 1985;58(3):350–6.
31. Grey IE, Li C, Madsen IC, Watts JA. The stability and structure of $Cs_x[Ti_{2-x/4}\square_{x/4}]O_4$, $0.61 < x < 0.65$. J Solid State Chem. 1987;66(1):7–19.
32. Kwiatkowska J, Grey IE, Madsen IC, Bursill LA. An x-ray and neutron-diffraction study of $Cs_2Ti_5O_{11}$ and Cs2Ti5O11.X2O, X = H, D. Acta Crystallogr B Struct Commun. 1987;43:258–65.
33. Bursill LA, Smith DJ, Kwiatkowska J. Identifying characteristics of the fibrous cesium titanate $Cs_2Ti_5O_{11}$. J Solid State Chem. 1987;69(2):360–8.
34. Peres V, Fabry P, Genet F, Dehaudt P. Preparations and characterizations of ceramics based on cesium titanate. J Eur Ceram Soc. 1994;13(5):403–10.
35. Kobyakov VP, Barinova TV, Sichinava MA. Phase relations in the TiO_2–$CsNO_3$ system between 550 and 1140 K. Inorg Mater. 2011;47(3):290–5.
36. Lu XG, Jin ZP. Thermodynamic assessment of the BaO-TiO_2 quasibinary system. Calphad. 2000;24(3):319–38.
37. Sanderson RT. Chemical periodicity, 1st edn. New York, NY: Reinhold Publishing Corporation; 1960.
38. Whaley TP. 8 - Sodium, potassium, rubidium, cesium and francium. In Hart WA, Beumel OF, Whaley TP, editors. The chemistry of lithium, sodium, potassium, rubidium, cesium and francium: Pergamon, Turkey, 1973; p. 369–529.
39. Parr RG. Density functional theory. Annu Rev Phys Chem. 1983;34:631–56.
40. Parr RG, Yang WT. Density-functional theory of the electronic structure of molecules. Annu Rev Phys Chem. 1995;46:701–28.
41. Wu LL, Schliesser J, Woodfield BF, Xu HW, Navrotsky A. Heat capacities, standard entropies and Gibbs energies of Sr-, Rb- and Cs-substituted barium aluminotitanate hollandites. J Chem Thermodyn. 2016;93:1–7.
42. Bale CW, Bélisle E, Chartrand P, Decterov SA, Eriksson G, Gheribi Ae, et al. FactSage thermochemical software and databases, 2010–2016. Calphad. 2016;54:35–53.
43. Utlak SA, Besmann TM. Thermodynamic assessment of the pseudoternary Na_2O-Al_2O_3-SiO_2 system. J Am Ceram Soc. 2018;101(2):928–48.
44. DeHoff R. Thermodynamics in materials science, 2nd edn. Boca Raton, FL: CRC Press; 2006.
45. Hanaor D, Sorrell CC. Review of the anatase to rutile phase transformation. J Mater Sci. 2011;46(4):855–74.

46. Eriksson G, Pelton AD. Critical evaluation and optimization of the thermodynamic properties and phase diagrams of the Mn–TiO_2, MgO–TiO_2, FeO–TiO_2, Ti_2O_3–TiO_2, Na_2O–TiO_2, and K_2O–TiO_2 systems. Metall Trans B. 1993;24(5):795–805.
47. Karkhanavala MD, Momin AC. Subsolidus reactions in the system Fe_2O_3-TiO_2. J Am Ceram Soc. 1959;42(8):399–402.
48. Cheynet B, Chaud P, Chevalier PY, Fischer E, Mason P, Mignanelli M. NUCLEA - thermodynamic properties and phase equilibria in nuclear systems. J Phys IV. 2004;113:61–4.
49. Fischer WA, Hoffmann A. The state diagram iron oxide-aluminum oxide. Arch Eisenhuttenwes. 1956;27(5):343–6.
50. Rosenbach K, Schmitz JA. Investigations in the ternary-system iron(II)-oxide-chromium(III)-oxide-alumina. Arch Eisenhuttenwes. 1974;45(12):843–7.
51. Eriksson G, Wu P, Pelton AD. Critical evaluation and optimization of the thermodynamic properties and phase diagrams of the MgO–Al_2O_3, MnO–Al_2O_3, FeO–Al_2O_3, Na_2O–Al_2O_3 and K_2O–Al_2O_3 systems. Calphad. 1993;17(2):189–205.
52. Stahleisen V, Eisenhüttenleute VD. Slag atlas, 2nd edn. Dusseldorf, Germany: Verlag Stahleisen GmbH; 1995.
53. Vidacak B, Sichen D, Seetharaman S. The existence of a ternary phase in the Al_2O_3–CaO–FeO system. ISIJ Int. 2002;42(5):561–3.
54. Dreval L, Zienert T, Fabrichnaya O. Calculated phase diagrams and thermodynamic properties of the Al_2O_3-Fe_2O_3-FeO system. J Alloy Compd. 2016;657:192–214.
55. Chase MW. NIST-JANAF thermochemical tables, 4th edn. Melville, NY: American Institute of Physics; 1998.
56. Kopp III H. Investigations of the specific heat of solid bodies. Phil Trans. 1865;155:71–202.
57. Latimer WM. Methods of estimating the entropies of solid compounds. J Am Chem Soc. 1951;73(4):1480–2.
58. Spencer PJ. Estimation of thermodynamic data for metallurgical applications. Thermochim Acta. 1997;314(1-2):1–21.

SUPPORTING INFORMATION

Additional supporting information may be found online in the Supporting Information section at the end of the article.

How to cite this article: Utlak SA, Besmann TM, Brinkman KS, Amoroso JW. Thermodynamic assessment of the hollandite high-level radioactive waste form. *J Am Ceram Soc*. 2019;00:1–14. https://doi.org/10.1111/jace.16438